Nonlinear Phenomena in Complex Systems, vol. **26**, no. 2 (2023), pp. 191 - 208

Plasmonic Metallic Carbon Nanotube Assemblies Enhancing Raman Optical Activity of DNA for Ultra-Sensitive Detection of KRAS-Gene Point Mutations

V. P. Egorova*
Belarusian Pedagogical State University, 18 Sovetskaja Str, 220050 Minsk, BELARUS

H. V. Grushevskaya†
Physics Department, Belarusian State University, 4 Nezalezhnasti Ave., 220030 Minsk, BELARUS

N. G. Krylova‡
Belarusian State Agrarian Technical University, 99 Nezavisimosti Ave., 220023 Minsk, BELARUS

E. V. Vaskovtsev§
Belarusian Pedagogical State University, 18 Sovetskaja Str, 220050 Minsk, The Republic of Belarus

A. S. Babenka¶
Belarusian State Medical University, 83 Dzerzhinski Ave., 220116 Minsk, BELARUS

G. G. Krylov**
Physics Department, Belarusian State University, 4 Nezalezhnasti Ave., 220030 Minsk, The Republic of Belarus

I. V. Anufreyonak††
N.N. Alexandrov National Cancer Center of Belarus, Lesnoy, Minsk District, 223040, The Republic of Belarus

S. Yu. Smirnov‡‡
N. N. Alexandrov National Cancer Center of Belarus, Lesnoy, Minsk District, 223040, The Republic of Belarus
(Received 17 January, 2023)

Highly sensitive methods of chiral Raman optics that allow to record conformational dynamics of deoxyribonucleic acid (DNA) molecules are promising for discrimination of somatic point mutations in the genome of colorectal cancer. The results of the sequencing are important for the correct drug prescription. However, it is challenging due to very low signal intensity of Raman optical activity of DNA. We offer a novel KRAS gene sequencing method which is based on the dependence of Raman band enhancement by plasmonic carbon nanotube assemblies on the DNA helicoidality degree and which registers the change of the DNA Raman optical activity due to formation of a homoduplex between complementary probe and target DNAs. We demonstrate that such a technology is very sensitive one when studying the allele single-nucleotide polymorphism of tumor genome.

PACS numbers: 88.30.rh, 87.15.Qt, 87.14.gk, 33.55.Be, 36.20.Ng
Keywords: carbon nanotube, DNA sensing, Raman optical activity, KRAS gene polymorphism
DOI: https://doi.org/10.33581/1561-4085-2023-26-2-191-208

1. Introduction

Currently, the development of nanosensors which are capable of detecting somatic point mutations (single base genomic variants, single nucleotide substitutions, single-nucleotide polymorphism (SNP)) in the genome of cancer patients is of great interest for medical applications. In oncology, the type of tumor molecular profile determines the choice of a treatment strategy which excludes the development of resistance to anticancer drugs [1]. Changes in DNA sequence of the oncogene of KRAS protein in the tumor genome of colorectal cancer correlate to a malignant state of the tumor. The difficulty of sequencing this gene is stipulated by the simultaneous presence of a reference wild-type allele as well as an alternative allelic variants (mutant-type allele) in the DNA sample. Besides, the process of tumor evolution is characterized by a variant history with the emergence as well of unknown point mutations. The method of determination of unknown mutations is based on sensitivity of the parameters of the unwinding and denaturation of the double-stranded DNA to its nucleotide composition, for example, such a parameter may be the melting point [2].

Chiral molecules, including biomolecules (helical double-stranded deoxyribonucleic acids (dsDNAs) and proteins), with a helical backbone are optically active ones [3]. DNA molecules comprise asymmetric sugars (deoxyribose) that cause the optical activity. After elastic (Raman) scattering of a laser beam on the molecules, the light gains an additional circularly polarized component due to their vibrational optical activity. It means that the plane of the electric field vector, $\vec{E}$, of the light wave, and, correspondingly, $\vec{E}$ is rotated by some angle. The enhanced sensitivity of the chiral-spectral method of Raman optical activity (ROA) is used to study structure and conformational dynamics of proteins in solutions [4]. ROA of DNA is sensitive to the conformal changes in the DNA structure [5, 6]. Generally, the drawback of Raman spectroscopy for DNA low-concentration measurements is low intensity of light scattering in DNA and, moreover, ROA is often only $10^{-3} - 10^{-5}$ times that of the Raman scattering intensity. Plasmonic nanoparticles that induce optical chiral field in the near-field area are capable of enhancing the intensity of the ROA spectra [7]. The signal-enhancement techniques are based on surface plasmon resonance phenomena [8]. The plasmon resonance occurs in close proximity to the surface of metal nanoparticles (gold nanoparticles) because the electric field from plasmonic monolayers of gold nanoparticles is distributed over a distance on the order of 250 nm from the gold-particle surface [9]. It means that the Raman scattering of light in DNA can only be enhanced in nanoscale region, e.g. in plasmonic nanopore array [10]. However, the long DNA molecules are extended beyond the near-field region, even if DNA polymerase amplification occurs in nanopores [11].

One way to solve the problem of holding DNA molecules at the surface of plasmonic particles is their non-covalent binding. However, additionally to the scattering of light in DNA, the surface scattering of light in impurities of external environment occurs. Since the DNA diameter is of 2 nm, the intensity of Raman scattering of light in DNA is less than 1% of the total Raman scattering level in the near-field region with a width of 250 nm.

Since the near-field region for graphene is 50-100 times smaller (on the order of $2.5 - 5$ nm) than for gold nanoparticles the signal-to-noise ratio in the Raman genosensor could be increased using the graphene [9]. Rolled up graphene sheets, called carbon nanotubes, are a promising material for constructing transducers based on

*E-mail: egorova_vp@bspu.by
†E-mail: grushevskaja@bsu.by
‡E-mail: nina-kr@tut.by
§E-mail: vaskovcev@mail.ru
¶E-mail: labmdbt@gmail.com
**E-mail: krylov@bsu.by
††E-mail: klaksa_06@mail.ru
‡‡E-mail: rustledeath24@gmail.com

changing of the redox properties of purine nucleotide bases, such as guanin for recording signal of hybridization between complementary electroactive DNA targets and probes [12].

In this paper, we propose to use few-walled carbon nanotubes to enhance the intensity of the circularly polarized component of laser beam Raman-scattered in helical DNA. A hybridization-signal optical transducer which enhances the Raman optical activity of DNA entering conjugates with CNTs will be based on high-ordered few-walled CNT assemblies. To construct the CNT-based optical transducer we employ a Langmuir–Blodgett (LB) technique which allows to fabricate highly ordered defect-free layered nanocomposites based on carbon nanotubes of very small diameters. In [13–16] the LB technique has been utilized to fabricate the crystalline CNT assemblies for plasmon applications. When creating a network the complexification between the highly-ordered carbon-nanotube arrays and dsDNA target molecules do not impair but improve the ability of the CNT arrays to screen electric fields [17, 18]. When decorating CNTs a high-conductive oligomer with conjugated double bonds enhances the efficiency of the screening by the highly-ordered CNT arrays [19, 20]. The Raman optical activity method will be used to perform an allele discrimination of a single nucleotide substitution in exon 2 codon 12 of the KRAS gene. This point mutation is the most common somatic mutation in the KRAS oncogene. The goal of the paper is to develop a method for detecting single nucleotide polymorphism of genome as a changing in Raman optical activity of the double DNA helix during its unwinding, followed by hybridization with oligonucleotides entering conjugates with few-walled carbon nanotube assemblies.

2. Materials and methods

2.1. Reagents for direct hybridization-mediated tumor-SNP detection

2.1.1. Native DNA from tissue samples

The native DNA molecules were isolated from human placenta, formalin-fixed paraffine-embedded (FFPE) tissue samples of colorectal cancer, and blood of colorectal-cancer patients, and rat glioma C6 cell line. The dsDNA has been purified from contaminating ribonucleic acids (RNA), ssDNA, proteins and lipids. In what follows, the placental dsDNA, the dsDNA of C6 cells, the dsDNA from the blood and the tumor tissue are denoted by $\mathrm{dsDNA_{pl}}$, $\mathrm{dsDNA_{C6}}$, $\mathrm{dsDNA_{bl}}$, and $\mathrm{dsDNA_{CRC}}$, respectively. The following KRAS variant: rs121913529 c.35G>A site, p.G12D, located in the second exon of the human KRAS gene (NCBI/Gene KRAS genomic DNA sequence NC_000012.12; NCBI/Gene KRAS mRNA var d sequence NM_001369787.1) is genotyped.

The C6 cells have been cultured in standard conditions. Clinical samples were collected at the N. N. Alexandrov National Cancer Center of Belarus. The study included 10 FFPE samples obtained from patients with advanced colon cancer. For isolation, 2–3 sections of the paraffin block were used. Deparaffinization was performed with xylene followed by washing with ethanol (95%). Total DNA isolation was performed using the QIAamp DNA FFPE Tissue Kit (Qiagen) according to the manufacturer's protocol.

The $\mathrm{dsDNA_{pl}}$ was isolated from placenta tissue of healthy donors. RNA and proteins contents in the high purity $\mathrm{dsDNA_{C6}}$ and $\mathrm{dsDNA_{pl}}$ (1.03 mg/ml in 10^{-5} M Na_2CO_3 buffer medium) were less that 0.1 % (optical density ratio $D_{260}/D_{230} = 2.378$ and $D_{260}/D_{280} = 1.866$, respectively).

The placental dsDNA has been used as a control perfect DNA of non-mutant (wild) type.

2.1.2. Model target ssDNAs

The 35-nucleotide sequences of the KRAS oncogene used as model DNA targets formed homoduplexes or heteroduplexes with 57% content of guanine-cytosine (G-C) pairs. The 35-base oligonucleotide denoted by "N3" being the perfect-matched KRAS-gene sequence has been used as a wild-type model target ssDNA. The 35-base oligonucleotide denoted by "M3" being the single base-mismatched KRAS-gene sequences has been used as a mutant model target ssDNA. The oligonucleotide M3 differs from the normal wild-type KRAS sequence by the nucleotide change in position 3.

2.1.3. Single-stranded hybridization ssDNA probes

The 19- and 20-base oligonucleotides, KRAS_w and KRAS_m, were utilized as short primers of wild- (reference, normal, non-mutant) and mutant- (alternative) type to the KRAS-gene, respectively. The perfect-matched (KRASw) and single base-mismatched (KRASm) probes are complementary to the KRAS-gene wild-type (normal, non-mutant) and mutant-type nucleotide sequences, respectively. The oligonucleotides KRASw and KRASm differ by the nucleotide change in position 12.

2.1.4. Toehold-mediated hybridization dsDNA probes

Conjugates of few-walled carbon nanotubes (FWCNTs) with double-stranded nucleotide sequences called double-stranded (toehold exchange) DNA, PF3/W3, were used to probe the model target DNA. The dsDNA probe can form a homoduplex with the complementary DNA target N3 or a heteroduplex with the single-nucleotide mismatched DNA target M3 in a reaction of displacement of the shorter protector oligonucleotide of the dsDNA probe (strand displacement reaction).

The PF3/W3 toehold duplex consisted of the two 35-base and 28-base oligonucleotides. The longer capture oligonucleotides, W3, is complementary to the wild KRAS gene. The four inosines replace guanines in the shorter chain, W3, being protector of the capture oligonucleotide "PF3". In the electrophoretic studies, the probe oligonucleotide (PF3) complementary to the protector strand was chemically labeled with a fluorescent group (fluorescein phosphoramidite, FAM).

The toehold exchange probe was fabricated by annealing the protector strand W3 with the complementary strand PF3 in TE buffer at 37 ± 0.1 °C. The strand displacement reaction proceeds during 1.5 hour through successively linking the nucleotides of the recognized ssDNA target to the longer capture complementary ssDNA chain from the dsDNA probe. The synthesis of the FWCNT conjugates lasted 30 minutes.

All oligonucleotides were purchased from "Primetech ALC" (Minsk, Belarus). The details of the sequences are listed in Table 1.

2.2. Materials for hybridization signal transducer

The carboxylated and stearic-acid-functionalized FWCNTs of 2.5 nm in diameter have been decorated by the cyclic complexes of Ce and/or high-spin octahedral Fe(II) with 3-hexadecyl-2,5-di(2-thienyl)-1H-pyrrole (H-DTP, H-dithienylpyrrole) ligands [21]. The H-DTP is an amphiphilic conducting oligomer of thiophene-pyrrole derivatives. An alkyl 16-link hydrocarbon chain $R = \mathrm{C_{16}H_{33}}$ was chemically bounded to the oligomer. Inverse micelles of stearic acid with DNA–FWCNT conjugates or DNA inside (called micellar DNA–FWCNT hybrids and micellar DNA) are obtained by mixing stearic acid with the appropriate reagent dissolved in hexane by the ultrasound treatment.

Salts $\mathrm{Fe(NO_3)_3 \cdot 9H_2O}$, $\mathrm{Ce_2(SO_4)_3}$ (Sigma, USA), hydrochloric acid, deionized water with resistivity of 18.2 MΩ·cm were used to preparate

Table 1: Sequences of all the oligonucleotides used in this study.

Name	Sequence structure ($5' \to 3'$)
N3	TGGTGGCGTAGGCAAGAGTGCCTTGACGATACAGC
W3	TGGTGICGTAGICAAGAITGCCTTIACG
M3	TG**A**TGGCGTAGGCAAGAGTGCCTTGACGATACAGC
PF3	GCTGTATCGTCAAGGCACTCTTGCCTACGCCACCA-FAM
$KRAS_w$	GTTGGAGCTGGTGGCGTAG
$KRAS_m$	AGTTGGAGCTG**A**TGGCGTAG

subphases. All chemical reagents of analytical grade were used without further purification.

2.3. Methods

2.3.1. Fabrication of dithienylpyrrole-coated CNT assemblies

By employing the LB technique, monomolecular crystalline DNA–CNT hybrid layers (DNA–CNT hybrid crystalline monolayers) were fabricated by compressing two-dimensional gas of inverse stearic-acid micelles with the carboxylated FWCNTs and DNA probe molecules inside. The hexane solution of the micellar DNA–FWCNT hybrids was preliminary dropped on deionized-water surface. Then the two DNA–CNT hybrid LB-monolayers were formed and deposited onto surface of nanoporous anodic aluminium oxide (AAO) with 10-nm pores or Si supports.

Preliminary, five iron-containing LB-monolayers consisting of the cyclic complex (Fe(II)DTP) of octahedral high spin Fe(II) with DTP ligands were formed. The FWCNTs were decorated by the nanocyclic organometallic LB-complexes. The CNT LB-arrays decorated by the dithienylpyrrole complexes of octahedral high spin Fe(II) host spin-polarized graphene charge carriers ([14, 15, 22]).

2.3.2. dsDNA denaturation

The target dsDNAs were denatured at 95 °C before detection. The denatured dsDNAs were hybridized with the ssDNA probes.

2.3.3. Raman spectroscopy

Spectral studies in visible range were carried out using a confocal micro-Raman spectrometer Nanofinder HE ("LOTIS-TII", Tokyo, Japan–Belarus) on diode-pumped solid-state (DPSS) lasers operating at wavelengths of 473, and 532 nm with power in the range from 0.0001 to 20 mW. The spectra were recorded in the back-scattering geometry under a $\times$ 50 objective at room temperature (RT). The size for the optical image is of 7×7 μm, vertical spatial resolution 150 nm, spectral resolution is of up to 0.01 nm.

2.3.4. Electrophoretic study

The electrophoresis (PAGE) was performed in polyacrylamide gel in 0.5$\times$ 0.09 M TBE buffer (pH 8.0) at room temperature during 45 min. Control of the electrophoretic system electrical parameters which are reset by power, was carried out on the equipment Electrophoresis Power Supply EPS 601 (GE Healthcare Bio-Sciences AB, Sweden). PAGE was repeated at least three times.

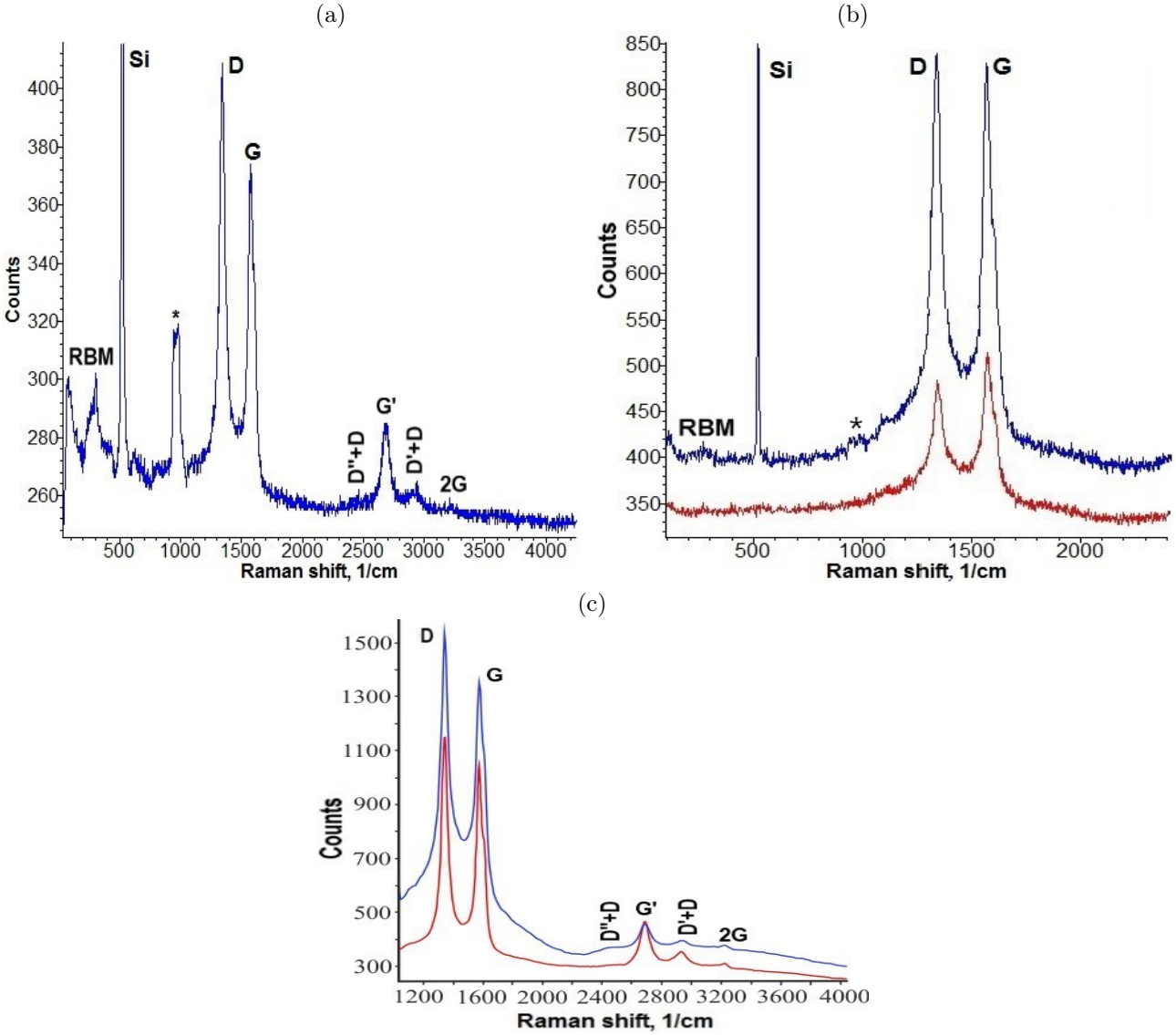

FIG. 1. Raman spectra: (a) stearic acid micelles with $dsDNA_{pl}$–FWCNTs inside; (b) the micellar $KRAS_w$–FWCNTs hybrids (red curve in figure b) and a crumpled (crushed) LB-monolayer formed of the stearic acid micelles with $KRAS_w$–FWCNTs hybrids inside (blue curve in figure b); (c) the LB-monolayer formed of the micellar $dsDNA_{pl}$-CNT hybrids with (c, blue curve) or without (c, red curve) propidium iodide. The micellar $KRAS_w$–FWCNT, $dsDNA_{pl}$–FWCNT hybrids, and the $KRAS_w$–FWCNT hybrid LB-monolayer were deposited on pure Si supports; the $dsDNA_{pl}$-CNT hybrid LB-monolayer was deposited on the Si support hydrophilized by H-DTP. The Raman spectra were recorded at laser excitation wavelength of 532 nm; the following laser powers and collected times were used for the specimen excitation: 20 mW and 1 s (figure a), 3 mW and 10 s (figures b and c).“*” denotes a laser mode.

3. Results

3.1. Raman spectral study of DNA–CNT hybrid interactions

3.1.1. Characterization of plasmonic CNT assembly

A prominent CNT radial breathing mode (RBM) of 298.28 cm^{-1} is featured in Raman

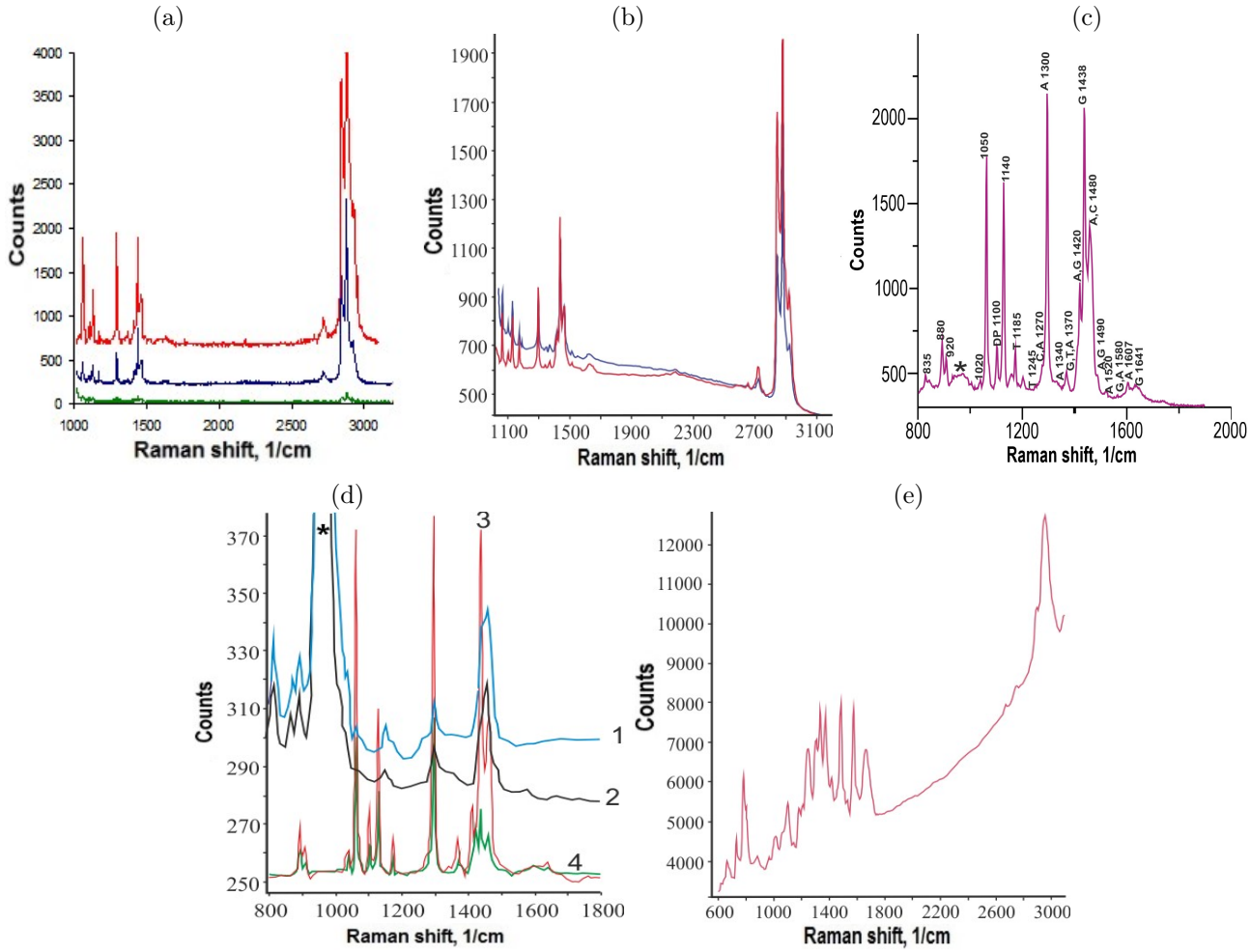

FIG. 2. (a) Raman spectra of pure stearic acid inverse micelles (green curve in figure a), the micelles with dsDNA$_{pl}$ inside (blue curve in figure a), the micelles with dsDNA$_{pl}$–FWCNTs inside (red curve in figure a); the pure stearic acid micelles and the micelles with dsDNA$_{pl}$ and dsDNA$_{pl}$–FWCNT hybrids inside were deposited on pure Si supports; the Raman spectra were recorded at laser excitation wavelength of 532 nm; the laser power and collected time were used for the specimen excitation: 2 mW and 60 s, respectively. (b) Raman spectra of the micellar dsDNA$_{C6}$ (red curve) and the micellar tumor dsDNA$_{CRC}$ (blue curve); the dsDNA$_{C6}$ and the dsDNA$_{CRC}$ were deposited on pure Si supports; the Raman spectra were recorded at laser excitation wavelength of 532 nm; the laser power and collected time were used for the specimen excitation: 2 mW and 60 s. (c) A Raman low-frequency part of the spectrum for the inverse micelles formed in hexane solution of mixture from stearic acid with dsDNA$_{pl}$ and dripped on pure Si. The numbers indicate the characteristic frequencies of dsDNA vibrations; adenine, guanine, thymine and cytosine are designated by A, G, T and C, respectively; DP denotes phosphodiester bond. Laser power, excitation wavelength, and collected time were of 20 mW, 532 nm, and 3 s, respectively. (d) Raman spectra of the micellar dsDNA$_{pl}$ (blue and black curves 1 and 2, respectively) and the micellar dsDNA$_{pl}$-CNT hybrids (red and green curves 3 and 4, respectively); the micellar dsDNA$_{pl}$ and dsDNA$_{pl}$-CNT hybrids were deposited on the Si hydrophilized by H-DTP; the Raman spectra were recorded at laser excitation wavelengths of 473 nm (curves 1 and 3) and 532 nm (curves 2 and 4), the following laser powers and collected times were used for the specimen excitation: 8 mW and 1 s (curves 1 and 3), 20 mW and 1 s (curves 2 and 4). (e) A Raman spectra of the original dry placental dsDNA$_{pl}$ deposited on pure Si support; the spectrum was recorded at laser excitation wavelengths of 473 nm; the laser power and collected time were used for the specimen excitation: 5.76 mW and 60 s. "*" denotes a laser mode.

spectra of the micellar CNTs (see Figs. 1a and 1b). Let us estimate the CNTs diameters using the formula (see ([23]), [24] and references therein)

$$\omega_{RBM} = \frac{C_t}{d_t}\sqrt{1 + C_{env}d_t^2} \qquad (3.1)$$

where C_{env} quantifies the environmental effect on the RBM frequency, C_t is empirically derived parameter (227 nm$\cdot$ cm^{-1}), d_t is a diameter of single-walled carbon nanotube (SWCNT) and is determined by the following formula:

$$d_t = \frac{a_{C-C}\sqrt{3}}{\pi}\sqrt{(n^2 + nm + m^2)}. \qquad (3.2)$$

Here the (n, m) integers are coordinates of a carbon-nanotube chiral vector, $\vec{C}_h$, determined by the following expression: $\vec{C}_h = n\vec{a}_1 + m\vec{a}_2$; $\vec{a}_1$ and $\vec{a}_2$ are hexagonal-lattice unit vectors; a carbon-carbon distance of the primitive graphene cell, a_{C-C}, is in the range from 1.42 Å (graphite) to 1.44 Å (C_{60}) (see [25–28] and references therein). Assuming that the C_{env} is approximately equal to zero for the stearic acid micelles with dsDNA-CNTs hybrids inside, the d_t being estimated by the eq. (3.1) for the RBM of 298.28 cm^{-1} is of 0.76 nm. CNTs with such diameter are single-walled carbon nanotubes. The (n, m) index being equal to $(7, 4)$ is a better fitting derived from eq. (3.2) for the a_{C-C} equal to 1.43 Å. For the (7,4) carbon nanotube, $n - m$ is a multiple of three: $n-m = 3q$ where q is an integer. It signifies that a one-dimensional Brillouin zone comprises $K(K')$ points of graphene Brillouin zone and, as a result, the carbon nanotubes are metallic with a band gap of 0 eV [29, 30]).

A so-called D peak in the Raman spectra is the defect-activated graphene band. The G peak is an in-plane vibrational mode that involves sp^2 hybridized carbon atoms that comprises the graphene sheet.

3.1.2. Characterization of CNT hybridization-signal transducer

The crystal structure of both the KRASw–SWCNT and dsDNA$_{pl}$–SWCNT LB-monolayers that are formed of the micellar KRAS$_w$–SWCNTs and dsDNA$_{pl}$–SWCNT conjugates, respectively, are broken when crumpling the LB-monolayers. Such structural defects appear also in CNTs when folding the KRASw–SWCNT and dsDNA$_{pl}$–SWCNT conjugates in the inverse micelles. As a result, since there are the structural defects in the rolled-up graphene sheets the defect-activated D band appears in the Raman spectra for the micellar DNA–SWCNT conjugates and the broken-down crumpled LB-films (see Fig. 1). Such regions of structural defects are called electrostatically-confined graphene $p - n$ $(n - p)$ junctions [16, 31].

A conformational state of dsDNA deposited on CNT can be investigated of exploiting propidium iodide (PI) being a DNA intercalating dye. The PI fluorescence grows when the PI molecules intercalate into the dsDNA helix. It is also used to indicate the presence of dsDNA. A Raman spectrum of scattered light for a PI-contained dsDNA$_{pl}$–CNT LB-conjugates is shown in Fig. 1c. The PI-fluorescence of the dsDNA$_{pl}$–CNT LB-conjugates indicates that PI is intercalated in the dsDNA$_{pl}$ and, correspondingly, the latter resides on the CNT walls in a double-helical state.

Since the metallic single-walled CNTs are flexible they can be arranged with a high degree of order. In this case, the D and G peaks can be very weak in the Raman spectra of DNA–CNT hybrids. A comparison between the Raman spectra for DNA-CNT conjugates in Fig. 1 and Figs. 2(a, red curve) and (d, red and green curves 3) testifies this disappearing. Prominent peaks in these Raman spectra in the Figs. 2(a, red curve) and (d, red and green curves 3 and 4)) indicate the DNA molecular group vibrations because their frequencies coincide with all characteristic bands of dsDNA in the recorded Raman DNA spectra presented in Figs. 2a, blue curve and 2b–d [17].

The Raman spectra of the dsDNA before and after its conjugation with the high-ordered arrays of the metallic SWCNTs are shown in Fig. 2a. Comparing the DNA Raman spectra in red and blue colors one can conclude that the

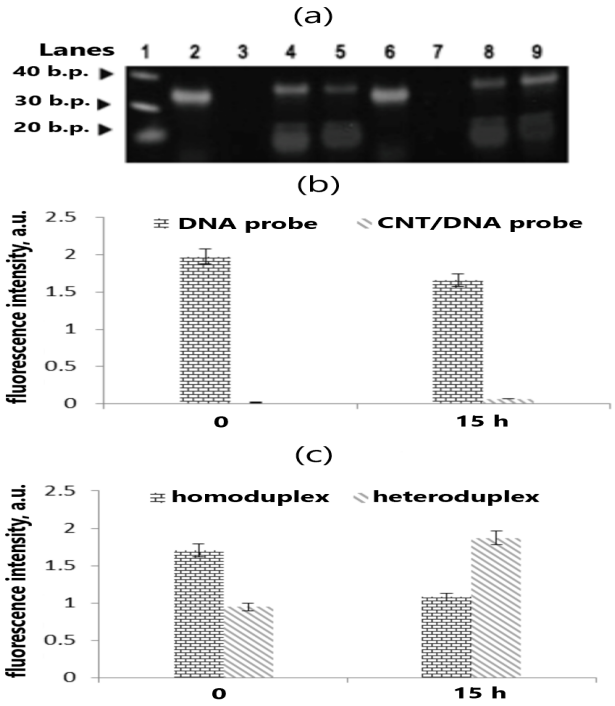

FIG. 3. Electrophoregram of mixture comprising FWCNTs and DNA. Lane 1 – marker (2 μg/ml); lanes 2 and 6 – toehold exchange probe PF3/W3 (1:2)(7 μl) just after synthesis and 15 hours later, respectively; Lanes 3 and 7 – conjugate FWCNT-PF3/W3 (7 μl) between FWCNTs and PF3/W3 (1:2) that is synthesized during 30 min and 15 hours, respectively; lanes 4 and 8 – conjugate FWCNT-PF3/N3 (7 μl) between FWCNTs and product (homoduplex PF3/N3) of hybridization reaction between PF3/W3 and N3 (1:4), that is synthesized during 30 min and 15 hours, respectively; lanes 5 and 9 – conjugate FWCNT-PF3/M3 (7 μl) between FWCNTs and product (heteroduplex PF3/M3) of hybridization reaction between PF3/W3 and M3 (1:4), that is synthesized during 30 min and 15 hours, respectively. The duration of the electrophoresis is of 2 hour at a bias voltage of 100 V, the FWCNT concentration is of 0.4 mg/ml. Insets (b) and (c) show intensity of the FAM fluorescence for the toehold exchange probe (lanes 2 and 6) and the duplexes of DNA target (lanes 4, 5, 8, and 9), respectively.

intensity of the DNA Raman bands is increased (see Fig. 2a). It signifies that the SWCNT micellar and LB assemblies possess plasmonic properties and, correspondingly, the assemblies can enhance the light scattering in the DNA in a result of plasmon resonance.

DNA Raman spectra are strongly affected by deprotonation. Due to the latter, the Raman spectral bands of DNA are widened even for a dry DNA sample (see the Raman spectrum of the dry $dsDNA_{pl}$ deposited on pure Si support in Fig. 2e). Hampering the deprotonation the stearic-acid shell of the inverse micelles drastically narrows Raman spectral bands in the Raman spectra for the micellar dsDNA and dsDNA–CNT hybrids deposited on pure Si (make comparison between the Raman spectra presented in Figs. 2a,b, and e).

Raman spectra for the micellar $dsDNA_{pl}$ dropped on a Si surface hydrophilized by the H-DTP molecules are significantly widened in comparison with the spectra of the micellar DNAs deposited on the non-modified Si surface (compare the two Raman spectra "1" and "2" shown in Fig. 2d with the Raman spectra in Figs. 2a, blue curve and b. However, the complexification of the $dsDNA_{pl}$ with the carbon nanotubes leads to the confinement of the placental DNA on the hydrophobic CNT surface by the $\pi - \pi$ stacking interactions

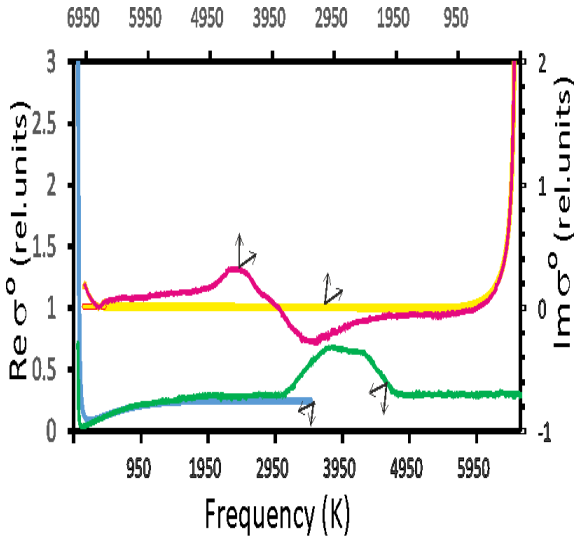

FIG. 4. Frequency dependencies of real (green and blue solid lines) and imaginary (yellow and magenta solid lines) parts of ohmic contribution $\sigma^{O}_{xx(yy)}$ to far-infrared conductivity in relative units of $e^2/\hbar$ for the graphene pseudo-Majorana fermion model (green and magenta lines) and for the Dirac massless fermion model [32, 33] (blue and yellow lines). Neglecting the pseudo-Majorana mass term the calculation was carried out at temperature of 200 K and the chemical potential of 33 K.

and, correspondingly, to a DNA protonation. The narrowing of the Raman spectrum of the micellar DNA_{pl}-CNT hybrids testifies the DNA protonation (make comparison between the values of spectral widths in the Raman spectra "1"–"4" shown in Fig. 2d).

3.1.3. Stability/reproducibility

The elecroforesis indicates quenching of FAM-fluorescence in PF3/W3 by FWCNTs during a long time period (15 hours and more) that testifies stability of the conjugates between FWCNTs and DNA (compare lanes 2 and 6 with lanes 3 and 7 in Fig. 3). A weakening of FAM-fluorescence quenching by carbon nanotubes in a result of PF3/N3 homoduplex formation is observed during 1.5 hour from the beginning of the strand displacement reaction (see Fig. 3, lanes 4 and 5). The observed weakening of the FAM-fluorescence CNT-quenching indicates a violation of the stacking interactions between the probe oligonucleotide and the carbon nanotubes (compare lanes 4 and 5 in Fig. 3). This weakening of FAM-fluorescence quenching is significantly less for the heteroduplex DNA, PF3/M3, than for the homoduplex DNA, PF3/N3 (compare lanes 4 and 5 in Fig. 3). The electrophoretic investigations shows that the strand exchange reaction with the formation of the duplex proceeds with a phase transition from the helical state of the DNA probe to the coil state, because the intensity of FAM-fluorescence increases with time due to the detachment of nucleotide bases from the CNT surface (compare lanes 5 and 9 in Fig. 3). The strand exchange reaction with the formation of a homoduplex begins with the phase transition from the helical state of the DNA probe to the coil state and ends with a phase transition of the homoduplex from the coil state to the double-helix state that is expressed in appearing a quenching of the homoduplex fluorescence 15 hours later (compare lanes 4 and 8 in Fig. 3).

3.2. Operating principles of metallic-CNT optical transducer of hybridization signal

Impressively fast response of the graphene sheets to the change of environment is provided by very high mobility of electrons and holes, being massless ones in valleys K and K' of graphene Brillouin zone. The K and K' are called Dirac points. A strongly interacting quasi-relativistic electron-hole plasma called a Dirac fluid exists in the vicinity of the Dirac point [34]. Non-Abelian statistics of the strongly correlated graphene charge carriers indicates their pseudo-Majorana vortical nature and, correspondingly, the pseudo-Majorana fermion graphene model is a topological semimetal (see [35–40]).

Confining pairwise the pseudo-Majorana fermions in the K and K' points the hexagonal symmetry of graphene lattice attributes negative and positive electrical charges, respectively, to

the bound (confined) pseudo-Majorana modes. Electromagnetic-field quanta are elastically (Compton) scattered on the vortical confined pseudo-Majorana modes. As a result, electron-hole pairs appear in the graphene conduction band. It signifies that graphene could efficiently screen applied electric fields.

When the electron and hole configurations are excited in flattened graphene bands, a deconfinement of the bound Majorana modes occurs. The deconfinement of the bound pseudo Majorana fermion in the graphene flat bands could significantly decrease the intensity of the elastic scattering because the deconfined pseudo Majorana fermions are electrically neutral. However, the presence of pseudo-Majorana mass term partially breaks the chiral symmetry of graphene in the flat bands. Due to the chiral anomaly, the electrically neutral pseudoMajorana fermions give avalanche-like rise to a huge number of electron-hole pairs [41]. Since the propagation pathes of the electrons and the holes along and against the applied electric field $\vec{E}$ do not coincide, a non-zero electric current flows in the graphene sheet. It means that 1) graphene can screen a low-frequency electrical fields similarly to a metal and 2) a free electron-hole pair density appears in the graphene conduction band in a result of the elastic (Compton) scattering of electromagnetic field quanta on the graphene electron density.

The zero-energy pseudo Majorana mode is a midgap state because the confinement (binding) of the pseudo fermions in the Dirac point, $K(K')$, occurs with forming the electron–hole configurations. A plasmon band in the spectrum of graphene optical conductivity appears due to the confinement.

When a monolayer of molecules is deposited on the graphene surface, the free vortical charge density is swinging on the eigenfrequencies of the molecule-nuclei vibrations in a response to electric fields of the nuclei oscillating in the molecular groups being adjacent to the graphene plane. The quantized collective oscillations are called plasmon modes. Zeros of the dielectric function for the pseudo-Majorana fermion model indicate that the collective modes in the massless Dirac plasma is an inherent feature of graphene (see Fig. 4) [35, 42].

An electrical field of scattered-light component, circularly polarized by spiralized dsDNA regions, twists the electrically charged density in graphene valleys K, K', where a zero-energy pseudo Majorana mode as a topological defect resides.

The zero-energy mode is the core of the vortex, and the swirling charge density plays the role of the "feathering" of this vortex. The emergent topologically non-trivial excitation of the Dirac fluid in the graphene sheet is the electron-hole configuration of bound (confined) pseudo Majorana particles.

The complementary region of the pure dsDNA forms a stable homoduplex with the ssDNA probe because the Helmholtz free energy of the complementary hybridized DNA probe and DNA target is less than the free energy of each on the CNT surface. The release of the oligonucleotide from the CNT surface with the formation of triplex regions in the target DNA violates the homogeneity of its helicoidal structure. Instead of a single double-helix twisted in one direction, many double-helix fragments appear with different helicity directions. The electromagnetic waves from the laser beam, after being elastically scattered by such partially untwisted pure DNA, are polarized in different directions so that the total polarization of the light decreases. Since the total circularly polarized component of the light scattered in DNA is small or absent, there is no swirling of the Dirac electron liquid in the graphene sheets and, correspondingly, the free graphene charge carriers (confined pseudo Majorana vortex-antivortex pairs similar to electron-hole pairs of nonzero energy) do not be exited. In the absence of plasma oscillations or their low intensity, the enhancement of light scattering in DNA on the CNT surface does not occur or is very weak.

The stacking interaction between $\pi(\mathrm{p}_z)$ electrons of CNT and DNA wraps the pure

dsDNA around the carbon nanotube. An increase in the intensity of light scattering in the dsDNA in a result of plasmon resonance testifies this winding.

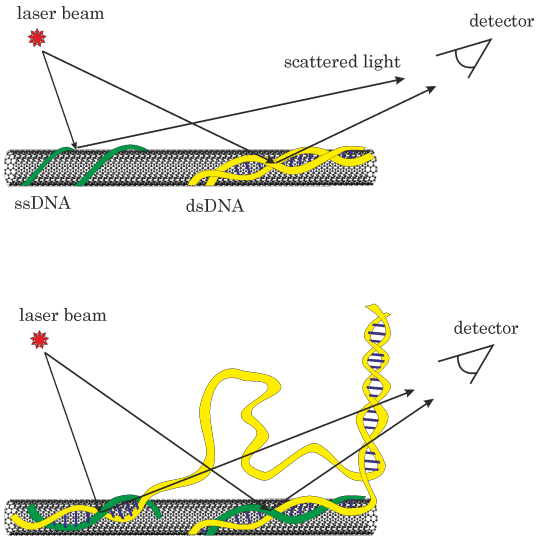

FIG. 5. Schematic of operating principle of DNA hybridization-signal transducer based on Raman optical activity: (up) optically highly active double-stranded DNA, which is fully double helix in the presence of non-complementary ssDNA probe; (down) optically low-active untwisted double-stranded DNA comprising double-stranded regions of different helicity and homoduplex between complementary ssDNA probe and chain of the dsDNA.

The conjugated-DNA hybridizing to complementary oligonucleotude probes forms homoduplexes [13]. The Raman genosensor operates on the effect of reducing the intensity of the helically polarized component of the DNA-scattered laser beam after homoduplexes formation. The operating principle of the genosensor are shown schematically in Fig. 5.

3.3. KRAS-gene sequencing based on both Raman optical activity of DNA and plasmon resonance

According to the Raman spectra shown in Figs. 6, the surface light-scattering enhancement decreases right until its disappearing after hybridization with a DNA probe whose nucleotide sequence matches that of the KRAS gene.

The micellar genotyping based on the plasmon-resonance effect and DNA ROA is performed in a following way. One detects a light scattering enhancement in duplexes between the target and probe DNAs and subsequently a dependence of this enhancement on the DNA–CNT hybrid type is analyzed. The intensity of the $KRAS_w$-$dsDNA_{C6}$-heteroduplex Raman bands (see the DNA peaks and the frequency region from 2700 to 3100 cm^{-1} in the Raman spectrum in light-blue, Fig. 6a) is significantly higher than one of the $KRAS_m$-$dsDNA_{C6}$-homoduplex Raman bands (see the frequency region from 2700 to 3100 cm^{-1} in the Raman spectrum in dark-blue, Fig. 6a). It testifies that the Raman optical activity of $dsDNA_{C6}$ being hybridized with $KRAS_w$ is better than ROA of the $dsDNA_{C6}$ being hybridized with $KRAS_m$ due to the fact that the $KRAS_m$-$dsDNA_{C6}$ hybrids are created in the result of the complementary hybridization. As it has been shown in Section 3.2 the decrease of the intensity of light scattering in the homoduplex DNA is stipulated by the diminishing of CNT-enhanced Raman scattering due to smaller numbers of graphene charge excitations because of smaller optical activity of the homoduplex DNA.

When forming a high-conducting network of CNTs linked by DNA molecules the complexification of highly-ordered CNT arrays with DNA does not impair but vice versa improves the plasmonic capability of the CNT arrays. The decreasing of Raman optical activity of DNA indicates that the $KRAS_m$-$dsDNA_{C6}$–CNT network is less perfect and when hybridizing the $KRAS_m$ primers and $dsDNA_{C6}$ molecules form homoduplexes.

The perfect plasmonic CNT assemblies with the high content of DNA and the low concentration of CNTs are formed in the presence of the homoduplexes $KRAS_w$-$dsDNA_{C6}$ because the the ration $\frac{I_D}{I_G}$ of intensities between the Raman D and G peaks is significantly less for the $KRAS_m$-$dsDNA_{C6}$ duplexes than for the $KRAS_w$-

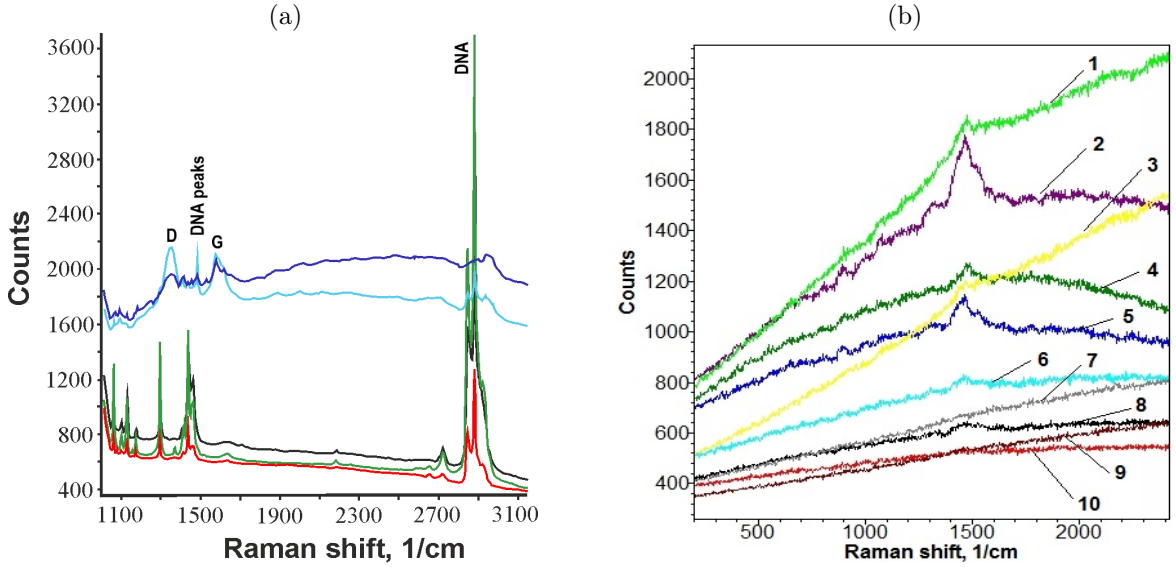

FIG. 6. Raman scattering genotyping. (a) Raman spectra of inverse micelles containing 1) DNA_{C6} isolated from C6-line cells (black curve), or 2) low-ordered FWCNT assembly covered by DNA molecules hybridized with $KRAS_w$- or $KRAS_m$-oligonucleotides (light- and dark blue curves, respectively), or 3) high-ordered FWCNT assembly covered by DNA molecules hybridized with $KRAS_w$- or $KRAS_m$-oligonucleotides (green and red curves, respectively). The spectra were recorded at laser excitation wavelengths of 532 nm; the laser power and collected time were used for the specimen excitation: 2 mW and 60 s, respectively. (b) Raman spectra of LB-FeDTP-film with oligonucleotide/SWCNT complexes after hybridization with dsDNA of different types: homoduplex of placental DNA with $KRAS_w$ (red curve (10)) and heteroduplex placental dsDNA with $KRAS_m$ (violet curve (2)) at excitation 532 nm; duplex (grey (7) and black (8) curves) of $KRAS_w$ and duplex (light-green (1) and green (4) curves) of $KRAS_m$ with $dsDNA_{bl}$ (at excitation at 473 and 532 nm, respectively); duplexes (blue curve (5) and light-blue curve (6)) between SNP-mutant $dsDNA_{CRC}$ and $KRAS_w$ or $KRAS_m$, respectively (at excitation at 532 nm); duplex (brown curve (9)) of $KRAS_w$ and duplex (yellow curve (3)) of $KRAS_m$ with the $dsDNA_{CRC}$ (excitation at 473 nm). Power was 0.6 mW for green laser and 0.24 mW for blue laser, accumulation time 10 s.

$dsDNA_{C6}$ duplexes (compare Raman spectra in light- and dark-blue, Fig. 6a). The decrease in the intensity of the DNA Raman peaks occurs due to the lower helicoidality of the untwisted dsDNA in the coil state when the conjugates are formed with a lower content of helical dsDNA and, correspondingly, the number of structural defects caused by the distortion of the graphene plane decreases. Thus, when creating the network the homoduplexes link the FWCNT together so that the degree of ordering of the CNT assemblies with the micellar DNA-CNT hybrids increases after the complementary hybridization.

Let us analyze the Raman spectra for conjugates of $KRAS_w$ probe-target dsDNA-FWCNTs with higher concentration of CNT and small concentration of DNA. The intensity of the DNA Raman bands of the conjugates is higher than the intensity of the Raman spectrum of the micelles with the original dsDNA (compare black and green curves in Fig. 6a). The FWCNT-enhanced light scattering in the dsDNA occurs due to the high Raman activity of the helical dsDNA. The intensity of the micellar DNA_{C6}–FWCNT-hybrid Raman bands for the homoduplexes, $dsDNA_{C6}$-$KRAS_m$, of the target $dsDNA_{C6}$ with the mutant-type probe, $KRAS_m$, is less than for the heteroduplexes, $dsDNA_{C6}$-$KRAS_w$, between the target $dsDNA_{C6}$ and the single base-mismatched oligonucleotide (as one can see from comparison between the Raman spectra in red and green, Fig. 6a). The

attenuation of plasmon resonance signifies that the ROA of the target DNA has decreased in a result of its transition to the partially untwisted state and, correspondingly, in a result of complementary binding to the probe DNA. According to these results, the KRAS gene of the cultured glioma cells has a point mutation of type of nucleotide substitution.

Let us study hybridization between the probe oligonucleotides and the placental DNA whose KRAS gene is of wild type always. The genotyping based on the plasmon-resonance effect and DNA ROA in LB DNA-CNT conjugates is performed in a following way. One detects the complementary DNA hybridization as a weakening of an enhancement of light scattering in the iron-contained dithienylpyrrole that is decorated the DNA-CNT LB-conjugates.

The weakening of plasmon resonance for the LB-CNT conjugates of DNA probe-dsDNA target duplexes and its complete absence for target DNA hybridizing to the probe DNA being conjugated with LB CNT assemblies testify that homoduplexes between $KRAS_w$ and $dsDNA_{pl}$ were formed (compare the Raman spectra in red and violet in Fig. 6b).

Now, one can discriminate the nucleotide sequence in the gene KRAS of the allele-SNP tumor genome. To do it, alternatively, the probe oligonucleotides $KRAS_w$ or $KRAS_m$ hybridize with the DNA samples from blood or tumor of colorectal-cancer patients. Let us compare the Raman spectra that were recorded at laser excitation with a wavelength 532 nm for the duplexes being formed after hybridization between the tumor DNA_{CRC} and $KRAS_w$ (the Raman spectrum (5) in blue) and between DNA_{CRC} and $KRAS_m$ (the Raman spectrum (6) in light-blue in Fig. 6b). The CNT enhancement of the light scattering in the dithienylpyrrole LB-monolayers decorating the CNT/oligonucleotide LB-assemblies is much less for the duplex $DNA_{CRC}/KRAS_w$ than for the heteroduplex of the placental wild-type $dsDNA_{pl}$ samples. Contrary to that, ROA of the duplex $dsDNA_{CRC}$ entering the conjugates CNT-$dsDNA_{CRC}$-$KRAS_m$ is much higher compared with the optical activity of the homoduplex $dsDNA_{pl}$ (make comparison between the Raman spectra (2),(10) in violet and red, respectively, and (5), (6) in blue and light-blue in Fig. 6b). Such behavior of the ROA is explained by the simultaneous presence of duplexes $KRAS_w/DNA_{CRC}$ and $KRAS_m/DNA_{CRC}$ and, correspondingly, testifies two types of alleles that is called SNP of gene KRAS in the tumor genome. The Raman spectra indicate decrease of optical activity of duplexes $KRAS_w/$ $dsDNA_{CRC}$ at excitation by 473-nm laser (see the Raman spectra (3) and (9) in yellow and brown, respectively, in Fig. 6b). This decrease can be explained by long-range charge transfer being more efficient for the double-helical heteroduplex DNA and less efficient one for partially-untwisted homoduplex DNA.

Let us analyze Raman spectra which were recorded at laser excitation at wavelength with 473 and 532 nm for the duplexes being formed after hybridization between the DNA_{bl}, isolated from the blood of colorectal-cancer patient and $KRAS_w$ (the Raman spectra (7) and (8) in gray and black, respectively, in Fig. 6b) and between DNA_{bl} and $KRAS_m$ (the Raman spectra (1) and (4) in light-green and green, respectively, in Fig. 6b). Similar as for DNA_{CRC}, both the duplexes $KRAS_w/DNA_{bl}$ and $KRAS_m/DNA_{bl}$ are optical active at 532-nm laser excitation. We observe also the decrease of optical activity of duplexes $KRAS_w/DNA_{bl}$ due to long-range charge transfer at excitation by 473 nm laser (see the Raman spectra (1) and (7) in light-green and green, respectively, in Fig. 6b).

Thus, the Raman spectra indicate the decrease of ROA for the duplexes of DNA_{CRC} and DNA_{bl} with both the oligonucleotide probes of wild and mutant types and, correspondingly, the performed spectral study confirms the allele SNP of the tumor genome. It signifies that both alleles of wild and mutant types present in the genome.

Thus, the sequencing method has allowed us to diagnose allele SNP of the KRAS-oncogene

in the genome of the colorectal cancer tissue. DNA molecules being non-specific linked to DNA probes are easily washed and do not contribute in the transducer response.

4. Discussion

The our results testify that the magnitude of the light-scattering enhancement in a result of plasmon resonance on the frequencies of vibrational modes for the molecules deposited on the rolled-up graphene-DNA monolayers depends on the magnitude of the Raman optical activity of dsDNA configuration. The experimental studies performed have revealed a large CNT light-scattering enhancement for the micellar helicoidal dsDNA. The intensity of Raman scattering in micellar homoduplexes is less than in heteroduplexes. The higher Raman optical activity of non-hybridized dsDNA remaining fully in a single helix double-stranded state in the presence of a non-complementary ssDNA probe, gives rise this enhancement effect of the heteroduplex formation. Complementary binding between dsDNA and the ssDNA probe causes a conformational transition of dsDNA to a state in which regions of different helicity are present, and, correspondingly, the homoduplex DNA in such an untwisted state becomes less optically active. The enhancement of Raman light scattering in the molecules located on graphene surfaces is explained by the existence of strongly correlated states (Dirac fluid) in the K, K' graphene valleys. We predict that these many-particle configurations are vortexes of graphene electron density and represent themselves topologically non-trivial defects of pseudo-Majorana nature. The circularly polarized component of the laser beam, twisting the electron density, excites pseudo Majorana modes in a bound (confined) state that are free electro-hole pairs in graphene.

The scattering of light in the aromatic molecular groups residing on the graphene plane is enhanced because the light is scattered on intensive graphene plasmonic oscillations emerging in a result of resonance with low-intensity vibrations of the aromatic molecular groups.

The novel high-performance ROA DNA sensor is capable of discriminating single-nucleotide polymorphism of KRAS gene in the human genome.

5. Conclusion

So, we offer a single molecular analysis that is based on the pseudo-Majorana fermion dispersion of the Dirac fluid in a graphene sheet. The physical fundamentals of the analysis are the excitation of plasmon modes in graphene. Their launch is performed by electromagnetic field quanta, circularly polarized in a result of scattering by optically active DNA molecules. The formation of homoduplexes is detected as an attenuation in the enhancement of Raman light scattering in the micelles comprised of complexes between pure DNA and FWCNTs as a result of plasmon resonance. An even greater decrease in the enhancement of Raman scattering up to the complete disappearance of SWCNT-enhanced Raman scattering in the decorating Fe(II)DPT monolayers deposited on the CNT LB-assemblies occurs during the formation of probe DNA homoduplexes from LB complexes between the oligonucletide and SWCNTs. This effect of Raman optical activity of DNA underlies the functioning of our Raman optical genosensor.

Our high-sensitivity ROA genosensor will be at an advantage over the plasmon-resonance sequencer when performing single-molecule allele discrimination of the genome of metastatic tumor cells at early and first stages of cancer.

References

[1] S. AlMusawi, M. Ahmed, and A. Nateri, Understanding cell-cell communication and signaling in the colorectal cancer microenvironment, Clin. Transl. Med. **11**, e308 (2021).

[2] K. Knez, D. Spasic, K. Janssen, and J. Lammertyn, Emerging technologies for hybridization based single nucleotide polymorphism detection, Analyst **139**, 353 (2014).

[3] L. Wang, N. Lu, S. Huang, M. Wang, X.-M. Chen, and H. Yang, Optically active nucleobase-functionalized polynorbornenes mimicking double-helix DNA, CCS Chem. **3**, 1787 (2021).

[4] F. Zhu, N. Isaacs, L. Hecht, and L. Barron, Raman optical activity: A tool for protein structure analysis, Structure **13**, 1409 (2005).

[5] M. Gąsior-Głogowska, K. Malek, G. Zajaca, and M. Baranska, A new insight into the interaction of cisplatin with DNA: ROA spectroscopic studies on the therapeutic effect of the drug, Analyst **141**, 291 (2016).

[6] L. Barron, The development of biomolecular Raman optical activity spectroscopy, Biomedical spectroscopy and imaging **4**, 223 (2015).

[7] S. Eslami and S. Palomba, Integrated enhanced Raman scattering: a review, Nano Convergence **8**, 41 (2021).

[8] A. Kakkanattu, N. Eerqing, S. Ghamari, and F. Vollmer, Review of optical sensing and manipulation of chiral molecules and nanostructures with the focus on plasmonic enhancements, Optics Express **29**, 12543 (2021).

[9] S. Huang, C. Song, G. Zhang, and H. Yan, Graphene plasmonics: physics and potential applications, Nanophotonics **6**, 1191 (2017).

[10] M. Iarossi, D. Darvill, A. Hubarevich, J.-A. Huang, Y. Zhao, A. De Fazio, D. O'Neill, F. Tantussi, and F. De Angelis, High-density plasmonic nanopores for DNA sensing at ultra-low concentrations by plasmon-enhanced Raman spectroscopy, Adv. Funct. Mater. , 2301934 (2023).

[11] S. Mao, J. Zhao, X. Ding, V. Vuong, J. Song, and L. Que, An integrated sensing chip for ultrasensitivity label-free detection of the products of loop-mediated isothermal amplification, ACS Sens. **8**, 2255 (2023).

[12] J. Rashida and N. Yusof, The strategies of DNA immobilization and hybridization detection mechanism in the construction of electrochemical DNA sensor: A review, Sensing and Bio-Sensing Res. **16**, 19 (2017).

[13] A. Egorov, V. Egorova, H. Grushevskaya, N. Krylova, I. Lipnevich, T. Orekhovskaja, and B. Shulitsky, CNT-enhanced Raman spectroscopy and its application: DNA detection and cell visualization, Letters in Applied NanoBioScience **5**, 346 (2016).

[14] H. Grushevskaya, N. Krylova, and I. Lipnevich, Enhancement of Raman light scattering in dye-labeled cell membrane on metal-containing conducting polymer film, Int. J. Mod. Phys. B **30**, 1642018 (2016).

[15] H. Grushevskaya, N. Krylova, I. Lipnevich, V. Egorova, and A. Babenko, Single nucleotide polymorphism genotyping using DNA sequencing on multiwalled carbon nanotubes monolayer by CNT-plasmon resonance, Int. J. Mod. Phys. B. **32**, 1840033 (2018).

[16] H. Grushevskaya and G. Krylov, Topologically tuned obliquity of klein-tunnelling charged currents through graphene electrostatically-confined p–n junctions, Int. J. Nonlinear Phenomena in Complex Syst. **25**, 21 (2022).

[17] A. Babenko, H. Grushevskaya, N. Krylova, I. Lipnevich, V. Egorova, and R. Chakukov, Nanopore-penetration sensing effects for target DNA sequencing via impedance difference between organometallic-complex-decorated carbon nanotubes with twisted single-stranded or double-stranded dna, in *Advanced Nanomaterials for Detection of CBRN, NATO Science for Peace and Security*, A: Chemistry and Biology., edited by J. Bonca and S. Kruchinin (Springer, Dorchester, 2020) pp. 247–258.

[18] H. Grushevskaya, N. Krylova, I. Lipnevich, A. Babenka, V. Egorova, and R. Chakukov, CNT-based label-free electrochemical sensing of native DNA with allele single nucleotide polymorphism, Semiconductors. **52**, 1836 (2018).

[19] H. Grushevskaya, I. Lipnevich, N. Krylova, and A. Babenko, Electrochemical impedance

spectroscopy sensing of viral DNA on surface of self-organized MWCNT-bundles decorated by organometallic complexes, in *Nonlinear phenomena in complex systems: Fractals, Chaos, Phase Transitions, Self-organization*, Nonlinear Dynamics and Applications, edited by V. I. Kuvshinov and S. V. A. (Pravo i Ekonomoka, Minsk, 2019) pp. 65–70.

[20] V. Egorova, H. Grushevskaya, A. Babenka, R. Chakukov, N. Krylova, I. Lipnevich, and E. Vaskovtsev, A single-molecule label-free identification of single-nucleotide colorectal-cancer-DNA polymorphism using impedance spectroscopy of self-redox-active decorated carbon nanotubes, Semiconductors. **54**, 1873 (2020).

[21] H. Grushevskaya, I. Lipnevich, and T. Orekhovskaya, Coordination interaction between rare earth and/or transition metal centers and thiophene series oligomer derivatives in ultrathin Langmuir-Blodgett films, J. Modern Physics. **4**, 7 (2013).

[22] H. Grushevskaya, N. Krylova, I. Lipnevich, T. Orekhovskaja, and B. Shulitski, Cell monolayer functioning detection based on quantum polarization effects in Langmuir-Blodgett multi-walled carbon nanotubes films, in *Nanomaterials for Security, NATO Science for Peace and Security*, A: Chemistry and Biology., edited by J. Bonca and S. Kruchinin (Springer, Dorchester, 2016) pp. 89–99.

[23] T. Araujo, P. Pesce, M. Dresselhaus, K. Sato, R. Saito, and A. Jorio, Resonance Raman spectroscopy of the radial breathing modes in carbon nanotubes, Physica E. **42**, 1251 (2010).

[24] A. Jorio and R. Saito, Raman spectroscopy for carbon nanotube applications, J. Appl. Phys. **129**, 021102 (2021).

[25] A. de Oliveira and C. Gonçalves Beatrice, Polymer nanocomposites with different types of nanofiller, in *Nanocomposites – Recent evolutions*, edited by S. Sivasankaran (IntechOpen, London, 2019) Chap. 6, p. 107.

[26] W. Choi and J. Lee, eds., *Graphene: Synthesis and applications* (ICRC Press, Abingdon, 2011).

[27] M. Monthioux, ed., *Carbon Meta-Nanotubes: Synthesis, Properties and Applications* (John Wiley & Sons, New Jersey, 2011).

[28] T. Kupka, M. Stachów, L. Stobiński, and J. Kaminský, Calculation of Raman parameters of real-size zigzag (n, 0) single walled carbon nanotubes using finite-size models, Phys.Chem.Chem.Phys. **18**, 25058 (2016).

[29] R. Saito and H. Kataura, Optical properties and Raman spectroscopy of carbon nanotubes, in *Carbon Nanotubes, Topics Appl. Phys.*, Vol. 80, edited by M. Dresselhaus, G. Dresselhaus, and P. Avouris (Springer-Verlag, Berlin, Heidelberg, 2001) Chap. 6, pp. 213–247.

[30] V. Gangoli, J. Azhang, T. Willett, S. Gelwick, E. Haroz, J. Kono, R. Hauge, and M. Wong, Using nonionic surfactants for production of semiconductor-type carbon nanotubes by gel-based affinity chromatography, Nanomater. Nanotechnol. **4**, 19 (2014).

[31] H. Grushevskaya, G. Krylov, S. Kruchinin, B. Vlahovic, and S. Bellucci, Electronic properties and quasi-zero-energy states of graphene quantum dots, Phys. Rev. B. **103**, 235102 (2021).

[32] L. Falkovsky, Optical properties of graphene and IV-VI semiconductors, Phys.-Usp. **51**, 887 (2008).

[33] L. Falkovsky and A. Varlamov, Space-time dispersion of graphene conductivity, Eur. Phys. J. **B56**, 281 (2007).

[34] J. Crossno, J. Shi, K. Wang, X. Liu, A. Harzheim, A. Lucas, S. Sachdev, P. Kim, T. Taniguchi, K. Watanabe, T. Ohki, and K. Fong, Observation of the Dirac fluid and the breakdown of the Wiedemann-Franz law in graphene, Science **351**, 1058 (2016).

[35] H. Grushevskaya and G. Krylov, Polarization in quasirelativistic graphene model with topologically non-trivial charge carriers, Quantum Rep. **4**, 1 (2022).

[36] H. Grushevskaya and G. Krylov, Semimetals with fermi velocity affected by exchange interactions: two dimensional Majorana charge carriers, Int. J. Nonlin. Phenom. in Complex Sys. **18**, 266 (2015).

[37] H. Grushevskaya, G. Krylov, V. Gaisyonok, and D. Serow, Symmetry of model N = 3 for graphene with charged pseudo-excitons, Int. J. Nonlin. Phenom. in Complex Sys. **18**, 81 (2015).

[38] H. Grushevskaya and G. Krylov, Electronic structure and transport in graphene: quasirelativistic Dirac-Hartree-Fock self-consistent field approximation, in *Graphene Science Handbook: Electrical and Optical Properties*, Vol. 3, edited by M. Aliofkhazraei, N. Ali, W. Milne, C. Ozkan, S. Mitura, and J. Gervasoni (Taylor and Francis Group, CRC Press, Boca Raton, 2016) pp. 117–132.

[39] H. Grushevskaya and G. Krylov, Massless Majorana-like charged carriers in two-dimensional semimetals, Symmetry. **8**, 60 (2016).

[40] H. Grushevskaya and G. Krylov, Vortex dynamics of charge carriers in the quasi-relativistic graphene model: high-energy $\vec{k} \cdot \vec{p}$ approximation, Symmetry. **12**, 261 (2020) .

[41] H. Grushevskaya, A. Timoshchenko, and I. Lipnevich, Topological defects created by gamma rays in a carbon nanotube bilayer, Nanomaterials **13**, 410 (2023) .

[42] H. Grushevskaya and G. Krylov, Anomalous charge transport properties and band flattening in graphene: a quasi-relativistic tight-binding study of pseudo-Majorana states, in *Graphene - A Wonder Material for Scientists and Engineers*, edited by M. Ikram, A. Maqsood, and A. Bashir (IntechOpen, London, 2023) Chap. 7, pp. 1–21